

# Atomic Description of the Interface between Silica and Alumina in Aluminosilicates through Dynamic Nuclear Polarization Surface-Enhanced NMR Spectroscopy and First-Principles Calculations

Maxence Valla,<sup>†</sup> Aaron J. Rossini,<sup>‡</sup> Maxime Caillot,<sup>§,||</sup> Céline Chizallet,<sup>||</sup> Pascal Raybaud,<sup>||</sup> Mathieu Digne,<sup>||</sup> Alexandra Chaumonnot,<sup>||</sup> Anne Lesage,<sup>#</sup> Lyndon Emsley,<sup>‡</sup> Jeroen A. van Bokhoven,<sup>\*,§,⊥</sup> and Christophe Copéret<sup>\*,†</sup>

<sup>†</sup>Department of Chemistry and Applied Biosciences, Laboratory of Inorganic Chemistry, ETH Zürich, Vladimir Prelog Weg 1-5, CH-8093 Zürich, Switzerland

<sup>‡</sup>Institut des Sciences et Ingénierie Chimiques, Ecole Polytechnique Fédérale de Lausanne (EPFL), CH-1015 Lausanne, Switzerland

<sup>§</sup>Department of Chemistry and Applied Biosciences, Institute for Chemical and Bioengineering, ETH Zürich, Vladimir Prelog Weg 1, CH-8093 Zürich, Switzerland

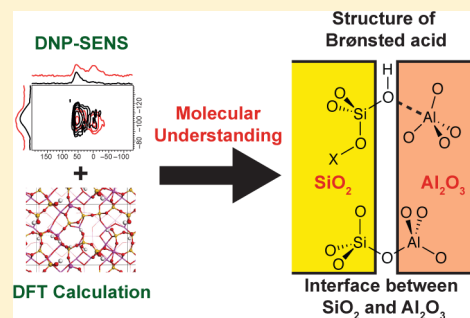
<sup>||</sup>IFP Energies nouvelles, Rond-point de l'échangeur de Solaize, BP 3, 69360 Solaize, France

<sup>⊥</sup>Paul Scherrer Institut, CH-5232 Villigen PSI, Switzerland

<sup>#</sup>Centre de RMN à Très Hauts Champs, Institut de Sciences Analytiques (CNRS/ENS Lyon/UCB Lyon 1), Université de Lyon, 69100 Villeurbanne, France

## S Supporting Information

**ABSTRACT:** Despite the widespread use of amorphous aluminosilicates (ASA) in various industrial catalysts, the nature of the interface between silica and alumina and the atomic structure of the catalytically active sites are still subject to debate. Here, by the use of dynamic nuclear polarization surface enhanced NMR spectroscopy (DNP SENS) and density functional theory (DFT) calculations, we show that on silica and alumina surfaces, molecular aluminum and silicon precursors are, respectively, preferentially grafted on sites that enable the formation of Al(IV) and Si(IV) interfacial sites. We also link the genesis of Brønsted acidity to the surface coverage of aluminum and silicon on silica and alumina, respectively.



## INTRODUCTION

Amorphous aluminosilicates (ASAs) are ubiquitous in catalysis and are used both as a catalyst and as a catalyst support for single sites, metal sulfides, and metal nanoparticles because they have high surface areas, combined with mild acidic properties alternative to zeolite in industrial reaction conditions.<sup>1–3</sup> They are known to dehydrate ethanol to ethylene, as well as to catalyze the isomerization of *m*-xylene.<sup>4</sup> They are also industrially used in refining technology to convert heavy fractions of crude oil and as supports for hydrotreating catalysts thanks to the tolerance of their acid sites to heteroelements containing organic molecules.<sup>5–8</sup> They also show promising properties in the production of fine chemicals<sup>1,2,9,10</sup> and the conversion of biomass.<sup>11,12</sup>

Their activity arises from their acid/base properties. The presence of both aluminum and silicon atoms at the surface of the materials induces Brønsted acidity to the surface hydroxyls.<sup>2,13–16</sup> However, the complex distribution of silicon and aluminum and the amorphous character of the material make the correlation between structure and activity very difficult to establish; the structure of the catalytically active sites are still a matter of debate.<sup>14,17–20</sup> The original structural models of ASA

proposed that the Brønsted acidity arises from protons compensating the electronic charge of the surface<sup>21,22</sup> or from HO–Al groups close to silanol groups.<sup>23</sup> Since these original pioneering works, numerous additional structural models have been proposed. Based on probe molecule adsorption, it has been suggested that the acidic sites are similar to those of zeolites, that is, bridging Si–OH–Al groups.<sup>14,20,24</sup> In contrast to depositing aluminum or silicon precursors, coimpregnation yields sites of similar strength as zeolites.<sup>16</sup> Other studies have concluded that the acidic sites are silanol groups in the vicinity of aluminum atoms (but not bridging the OH). In this case, the nature of Al atoms in the vicinity of the acidic groups is also a subject of discussion: tetrahedral Al(IV), five-coordinate Al(V),<sup>18,25</sup> and unsaturated Al(III) sites have all been proposed.<sup>17,18</sup> All these structural propositions are based on interpretation of complex spectral data. For instance, the assignments of OH infrared stretching frequencies have been debated.<sup>26–28</sup> In particular, the vibrational properties of probes such as CO and pyridine are not

Received: June 12, 2015

Published: August 5, 2015

unambiguously specific to given ASA surface sites.<sup>29,30</sup> Additionally, the numerous preparation routes give rise to a broad range of materials with varying structure, acidity, and active sites.<sup>16</sup> Even the surfaces that are formed using well-defined methods are heterogeneous in nature.<sup>16</sup> More recently, pseudo-bridging silanol groups have also been proposed to be active sites based on DFT calculations.<sup>19</sup>

An efficient synthesis of ASA materials involves the controlled grafting of aluminum alkoxide or silicon alkoxide precursors onto a silica or alumina surface under anhydrous conditions at low temperatures, thus forming  $\text{Al}_2\text{O}_3$  on  $\text{SiO}_2$  ( $\text{Al}/\text{SiO}_2$ ) and  $\text{SiO}_2$  on  $\text{Al}_2\text{O}_3$  ( $\text{Si}/\text{Al}_2\text{O}_3$ ), respectively.<sup>16,31–33</sup> This approach has the advantage of providing a homogeneous and regular deposition. The anhydrous conditions prevent the prehydrolysis of the precursor and inhomogeneous deposition. In addition, the amount of precursor grafted on the surface is mainly directed by the size of the alkyl chain of the precursor used. High Al and Si loadings may be achieved through successive grafting steps for both  $\text{Al}/\text{SiO}_2$  and  $\text{Si}/\text{Al}_2\text{O}_3$ . The stoichiometric adsorption and further dehydration of ethanol enabled the quantification of the surface density of active sites.<sup>33</sup> Even with a controlled deposition synthesis of ASA materials,  $\text{Si}/\text{Al}_2\text{O}_3$  and  $\text{Al}/\text{SiO}_2$  still have multiple types of Brønsted acid sites on their surface. Comparing these data to the catalytic activity for *m*-xylene isomerization revealed a moderate intrinsic acidity of these materials with respect to zeolites,  $\text{Si}/\text{Al}_2\text{O}_3$  being the more reactive.<sup>33</sup> Grafting of the silicon precursor occurred first on the (100) surface. Brønsted acidity only appeared upon grafting the (110) surface.<sup>8,32–34</sup>

While NMR spectroscopy is a valuable tool to obtain insights into the nature of Al and Si species on ASA,<sup>18,35–39</sup> unambiguous identification of the most relevant surface sites has not been achieved yet, one reason being the small amount of surface sites combined with the low sensitivity of NMR. Dynamic nuclear polarization surface enhanced spectroscopy (DNP SENS)<sup>40–42</sup> has recently been introduced to characterize materials and in particular their surfaces. In a DNP SENS experiment, the sample is impregnated with a small volume of a solution containing a persistent radical that acts as the DNP polarizing agent.<sup>40–42</sup> Impregnation brings the solvent and DNP polarizing agent (usually a nitroxide biradical)<sup>43</sup> into contact with the surface. DNP at low temperatures<sup>44,45</sup> (ca. 100 K) is then used to enhance the polarization of protons of the solvent and surface functionality.<sup>43–45</sup> The DNP enhanced proton polarization is then transferred to the surface heteronuclei by cross-polarization (CP)<sup>46</sup> or other coherence transfer methods.<sup>40–42,46–48</sup> For inorganic materials, signals from NMR active nuclei residing at the surface of the material are selectively enhanced since only the surface nuclei are in proximity to the protons of the solvent or surface functionalities. DNP SENS routinely provides sensitivity enhancements of 2 orders of magnitude,<sup>49,50</sup> enabling NMR experiments that would normally require isotopic labeling or prohibitively long signal averaging periods.<sup>40–42,48</sup>

Here, we apply DNP SENS for the detailed characterization of ASA materials prepared via controlled grafting approach, so as to provide an unambiguous characterization of the interface between silica and alumina for two well-defined series of samples: silica deposited on alumina ( $\text{Si}/\text{Al}_2\text{O}_3$ ) and alumina deposited on silica ( $\text{Al}/\text{SiO}_2$ ) materials.<sup>16</sup> DNP NMR has recently been applied to characterize materials such as alumina, silica, and  $\beta$ -zeolite surfaces.<sup>51–57</sup> Here DNP SENS allows sensitivity enhancements of several orders of magnitude, thus enabling the acquisition of natural abundance  $^{29}\text{Si}$ – $^{27}\text{Al}$  scalar

and dipolar heteronuclear correlation spectra, providing structural insight into the alumina/silica interface of these materials. Calculations of NMR signatures of surface sites of  $\text{Si}/\text{Al}_2\text{O}_3$  on a aluminosilicate model by periodic density functional theory (DFT) calculations, which have proven to be efficient for the assignment of NMR spectra of various oxides,<sup>58–66</sup> allow us not only to propose a structure for the interface between the alumina and the silica but also to propose structural models of the Brønsted acid sites of ASA.

## ■ EXPERIMENTAL AND COMPUTATIONAL DETAILS

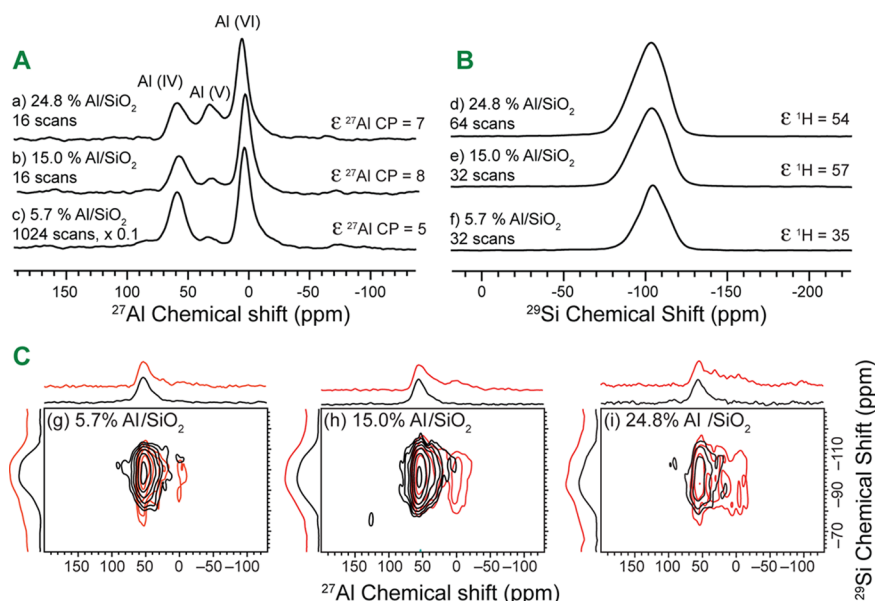
Samples were prepared by chemical liquid deposition (CLD) and exhibit different concentrations of  $\text{SiO}_2$  on  $\text{Al}_2\text{O}_3$  ( $\text{Si}/\text{Al}_2\text{O}_3$ ) and  $\text{Al}_2\text{O}_3$  on  $\text{SiO}_2$  ( $\text{Al}/\text{SiO}_2$ ) (Table 1).<sup>32</sup>  $\text{Si}/\text{Al}_2\text{O}_3$  samples were prepared by

Table 1. Properties of Synthesized ASA Materials<sup>16</sup>

number of grafting cycles	wt % of $\text{Al}_2\text{O}_3$ grafted on $\text{SiO}_2$ ( $\text{Al}/\text{SiO}_2$ )	wt % of $\text{SiO}_2$ grafted on $\text{Al}_2\text{O}_3$ ( $\text{Si}/\text{Al}_2\text{O}_3$ )
1	5.7	7.3
2	15.0	12.0
3	24.8	17.1

contacting excess tetraethyl-orthosilicate dissolved in dry toluene with alumina (resulting from calcination at 540 °C of Pural SB3, Sasol) in inert atmosphere (argon). After elimination of the unreacted precursor molecules, the samples were dried at 100 °C and further calcined at 500 °C under flow of air for 4 h. The 7.3 wt % of  $\text{SiO}_2$   $\text{Si}/\text{Al}_2\text{O}_3$  sample was obtained after one grafting step; 12.0 and 17.1 wt % of  $\text{SiO}_2$   $\text{Si}/\text{Al}_2\text{O}_3$  samples were obtained after completion of two and three grafting steps, respectively. In all cases, the final composition was determined by X-ray fluorescence spectroscopy. A similar procedure was applied for the preparation of the  $\text{Al}/\text{SiO}_2$  samples. Aluminum isopropoxide dissolved in dry toluene was contacted with silica in inert atmosphere (silica gel beads from Grace). The amount of aluminum precursor was adapted to obtain either 5.7 wt % of  $\text{Al}_2\text{O}_3$  or 15.0 wt % of  $\text{Al}_2\text{O}_3$  after one grafting step; 24.8 wt %  $\text{Al}/\text{SiO}_2$  was obtained after a second grafting step.

For DNP SENS<sup>40,42</sup> experiments, the nitroxide biradical polarizing agents bCTbK<sup>47</sup> or TEKPol were used.<sup>67</sup> Incipient wetness impregnation with 1,1,2,2-tetrachloroethane (TCE) biradical solution<sup>42,68</sup> with a concentration of 14–16 mM biradical was used to prepare the samples for DNP experiments. The impregnated samples were packed into sapphire rotors, and the sample was frozen at 100 K inside the low temperature 3.2 mm MAS probe head. Samples were typically subjected to multiple insert–eject cycles and left under an eject gas flow prior to insertion in order to reduce the amount of oxygen in the TCE solution and increase DNP enhancements.<sup>69</sup> Experiments were performed with a 400 MHz (9.4 T)/263 GHz Bruker DNP system or a 600 MHz (14.1 T)/395 GHz Bruker DNP system.<sup>70</sup> The sweep coil of the main magnetic field was set so that microwave irradiation occurred at the  $^1\text{H}$  positive enhancement maximum of nitroxide biradicals. Standard ramped cross-polarization (CP)<sup>46</sup> was then used to transfer polarization from the  $^1\text{H}$  nuclei to the nucleus of interest ( $^{29}\text{Si}$  or  $^{27}\text{Al}$ ). For  $^1\text{H}$ – $^{27}\text{Al}$  CP experiments, a low  $^{27}\text{Al}$  spin lock radiofrequency field less than 20 kHz was employed in order to maximize the efficiency of the CP transfers. Two-dimensional  $^{29}\text{Si}$ – $^{27}\text{Al}$  scalar correlation spectra were acquired with a refocused INEPT pulse sequence (Figure S1).  $^{29}\text{Si}$ – $^{27}\text{Al}$  dipolar correlation spectra were acquired with a dipolar refocused  $\text{R}^3$ -INEPT pulse sequence<sup>71</sup> where first order rotary resonance recoupling ( $\text{R}^3$ )<sup>72</sup> was employed to recouple  $^{29}\text{Si}$ – $^{27}\text{Al}$  dipolar couplings. In all cases, initial  $^{29}\text{Si}$  magnetization was generated with  $^1\text{H}$ – $^{29}\text{Si}$  CP with a 6 ms contact time. We also tested a  $^{29}\text{Si}$ – $^{27}\text{Al}$  population transfer-HMQC pulse sequences<sup>73</sup> (with detection of  $^{29}\text{Si}$ ) to obtain scalar correlation spectra; however, the INEPT type sequences (with  $^{27}\text{Al}$  detection) were found to provide superior sensitivity.  $^1\text{H}$ – $^{27}\text{Al}$  and  $^1\text{H}$ – $^{29}\text{Si}$  HETCOR experiments were performed with *e*-DUMBO<sub>1–22</sub> homonuclear decoupling applied during the  $t_1$  evolution period.<sup>74</sup> The States-TPPI procedure was applied to achieve quadrature detection in the indirect



**Figure 1.** (A) DNP enhanced  $^1\text{H}$ - $^{27}\text{Al}$  CPMAS solid-state NMR spectra acquired at 600 MHz/395 GHz: (a) 24.8 wt % Al/SiO<sub>2</sub>, (b) 15.0 wt % Al/SiO<sub>2</sub>, (c) 5.7 wt % Al/SiO<sub>2</sub>. Spectra for all of these samples were also measured on a 400 MHz DNP spectrometer (Figure S3, ESI). The recycle delay was 3.5 s. (B) DNP SENS (400 MHz/263 GHz)  $^1\text{H}$ - $^{29}\text{Si}$  CPMAS solid-state NMR spectra: (d) 24.8 wt % Al/SiO<sub>2</sub>, (e) 15.0 wt % Al/SiO<sub>2</sub>, (f) 5.7 wt % Al/SiO<sub>2</sub>. For  $^{29}\text{Si}$  measurement, DNP enhancement was measured by directly observing the  $^1\text{H}$  spectrum, since the acquisition of a  $^{29}\text{Si}$  CPMAS spectrum without DNP required too long for signal averaging. All spectra were acquired with a 12.5 kHz spinning frequency and a CP contact time of 0.6 ms for  $^{27}\text{Al}$  and 3.0 ms for  $^{29}\text{Si}$ .  $^1\text{H}$ - $^{29}\text{Si}$  CPMAS spectrum of the starting silica is available Figure S7. (C) DNP SENS (400 MHz/263 GHz) scalar refocused INEPT (black traces/contours) and dipolar refocused R<sup>3</sup>-INEPT (red traces/contours)  $^{29}\text{Si}$ - $^{27}\text{Al}$  heteronuclear correlation spectra: (g) 5.7 wt % Al/SiO<sub>2</sub>, (h) 15.0 wt % Al/SiO<sub>2</sub>, (i) 24.8 wt % Al/SiO<sub>2</sub>. All spectra were acquired with a 12.5 kHz MAS frequency. Projections of the 2D spectra are shown along the horizontal and vertical axes. For dipolar correlation experiments, 96 total rotor cycles ( $N$ , Figure S1) of recoupling were used, while for scalar correlation experiments, 420 total rotor cycles of evolution were used. Spectra were acquired with between 16 and 80 scans per increment, 28  $t_1$  increments, and a rotor synchronized  $t_1$  increment of 80  $\mu\text{s}$ . Recycle delays were optimized for sensitivity and were between 3.8 and 5.0 s. The pulse sequences used to acquire the 2D spectra are illustrated in Figure S1.

dimension. The one-dimensional  $^{27}\text{Al}$  DNP SENS CPMAS spectra were fit to a Cjzek model implemented in DMFit program in order to model the broad and featureless  $^{27}\text{Al}$  resonances characteristics of distributions of quadrupole and chemical shift parameters.<sup>75</sup> The fits enabled the determination of the relative ratio of each species, the isotropic chemical shift ( $\delta_{\text{iso}}$ ), the Gaussian distribution of the chemical shifts ( $\Delta\delta_{\text{iso}}$ ), and the quadrupolar coupling constant.

Density functional theory (DFT) calculations were performed starting from the periodic ASA model previously established,<sup>19</sup> according to a SiO<sub>2</sub>/Al<sub>2</sub>O<sub>3</sub> type, for  $\theta_{\text{OH}} = 5.4 \text{ nm}^{-2}$  and  $\theta_{\text{Si}} = 6.5 \text{ nm}^{-2}$ . This model was obtained by calculating the interaction of silicic compounds (silicic acid and a silica film) on a  $\gamma$ -Al<sub>2</sub>O<sub>3</sub> model previously described by Digne et al.<sup>76,77</sup> Molecular dynamics simulations revealed amorphization as well as mixing between the silica and alumina phases, by extraction of some aluminum atoms from the alumina layer to the silica one. The step-by-step simulation of hydration led to models containing OH groups. Shielding tensor computations were carried out with the CASTEP code,<sup>78</sup> using the generalized gradient approximation of Perdew, Burke, and Ernzerhof (PBE)<sup>79</sup> and ultrasoft pseudopotentials<sup>80</sup> (cutoff energy 550 eV). A  $1 \times 1 \times 2$   $k$ -points mesh was used. The gauge including projector augmented wave (GIPAW) algorithm<sup>81</sup> was applied. Due to computer memory constraints, the size of the systems modeled was reduced compared with the original geometry, by removing the lowermost atoms from the cell and saturating the resulting dangling bonds with water molecules to avoid unphysical electrostatic effects (Figure S2). The isotropic shielding ( $\sigma_{\text{iso}}$ ), quadrupolar coupling constants ( $C_Q$ ), and asymmetry parameters ( $\eta$ ) of  $^1\text{H}$ ,  $^{27}\text{Al}$ , and  $^{29}\text{Si}$  were calculated. Tetramethylsilane (for  $^1\text{H}$  and  $^{29}\text{Si}$ ) and  $\alpha$ -Al<sub>2</sub>O<sub>3</sub> (for  $^{27}\text{Al}$ ) were used as references for chemical shift calculations.

## RESULTS AND DISCUSSION

**Probing the Structure of Aluminum on SiO<sub>2</sub>.** The samples with increasing loadings of aluminum (i.e., 5.7, 15, and 24.8 wt % of Al<sub>2</sub>O<sub>3</sub> on SiO<sub>2</sub> noted Al/SiO<sub>2</sub>) were analyzed with  $^1\text{H}$ - $^{27}\text{Al}$  cross-polarization magic angle spinning (CPMAS) solid-state NMR spectroscopy. Indirect  $^1\text{H}$  DNP coupled with CPMAS enables the selective enhancement of the NMR signals of the surface  $^{27}\text{Al}$  nuclei that are nearby to  $^1\text{H}$  nuclei of the surface hydroxyl groups and solvent molecules.<sup>51</sup> Here a short contact time of 0.6 ms was employed in  $^1\text{H}$ - $^{27}\text{Al}$  CPMAS experiments since it is well-known that with short contact times the CP experiment is very selective and only nuclei in close proximity to protons will be excited. CP transfers to more distant subsurface will also be less efficient due to dipolar truncation, ensuring that only surface nuclei are detected.<sup>55</sup>  $^1\text{H}$  DNP enhancements were measured with CP to  $^{27}\text{Al}$  ( $\epsilon_{\text{Al-CP}}$ ) and were between 5 and 8 for the different samples at 600 MHz/395 GHz (Figure 1A, spectra a–c). Note that previous studies indicate that the overall sensitivity enhancement, compared with a dry sample at room temperature, is usually similar to the  $\epsilon$  value under these conditions.<sup>49</sup> DNP enhanced  $^1\text{H}$ - $^{27}\text{Al}$  CPMAS spectra were also acquired at 400 MHz/263 GHz, and higher ( $\epsilon_{\text{Al-CP}}$ ) signal enhancements between 51 and 80 were observed (Figure S3). The resolution of the  $^{27}\text{Al}$  solid-state NMR spectra is greatly improved at higher magnetic field, as expected for quadrupolar nuclei such as  $^{27}\text{Al}$ . Therefore, our analysis of 1D spectra focuses on the high field spectra.

In all samples, three peaks centered around 6, 33, and 60 ppm are assigned, respectively, to hexa-coordinated Al(VI), penta-



coordinated Al(V), and tetra-coordinated Al(IV) aluminum sites, similarly to what is observed for  $\gamma$ -alumina, albeit with a larger component of Al(V),<sup>51,66,82–84</sup> in agreement with previous NMR measurements.<sup>18,35,37,38</sup> The shape of the peaks in the spectra evolves as the concentration of alumina on  $\text{SiO}_2$  changes. We also note that as the Al loading increases, the intensity of the  $^{27}\text{Al}$  CPMAS spectra also substantially increases (Figure S3). The one-dimensional  $^{27}\text{Al}$  DNP SENS CPMAS spectra were fit to a Cjzek model implemented in DMFit program to model the broad and featureless  $^{27}\text{Al}$  resonances characteristics of distributions of quadrupole and chemical shift parameters (Figure S4).<sup>75</sup> The fits enabled the determination of the relative ratio of each species, the isotropic chemical shift, and the quadrupolar constant (Table S1 and Figure S5). The fits show that for Al/ $\text{SiO}_2$  the relative amount of Al(V) (2%, 11%, and 17%) increases with higher aluminum loading.

For Al/ $\text{SiO}_2$ , all of the 1D DNP enhanced  $^{29}\text{Si}$  CPMAS NMR spectra show a major peak centered at around  $-100$  ppm and a reduced intensity “tail” at around  $-85$  ppm (Figure 1B, spectra d–f). The major peak at  $-100$  ppm indicates that most silicon atoms are present as  $\text{Q}_4$  sites. As the aluminum loading increases the intensity of the tail increases and moves toward more positive chemical shift. Silicon with multiple neighboring aluminum atoms or protons bound to the coordinating oxygen atoms should exhibit more positive chemical shifts (see next section, regarding Si/ $\text{Al}_2\text{O}_3$  samples).<sup>4,85,86</sup> It is indeed well-known from experiments on crystalline materials that substitution of aluminum atoms into neighboring tetrahedral sites around tetrahedral silica induces a positive displacement of the  $^{29}\text{Si}$  chemical shift.<sup>85–89</sup> From solid-state NMR experiments performed on amorphous silica, it is also known that Si atoms with protons bound to coordinating oxygen atoms are also displaced to higher  $^{29}\text{Si}$  chemical shifts.<sup>4,85,86,90</sup> Finally, we note that 1D  $^{29}\text{Si}$  CPMAS experiments and 2D  $^{29}\text{Si}$ – $^{27}\text{Al}$  INEPT-HETCOR experiments used 3 and 6 ms contact times, respectively, since these relatively long contact times gave the most signal. However,  $^{29}\text{Si}$  CPMAS spectra of 17.1% Si/ $\text{Al}_2\text{O}_3$  acquired with contact times of 1–6 ms showed only minor variation in the observed  $^{29}\text{Si}$  chemical shifts with contact time (Figure S6). This suggests that even at relatively long contact times only the surface of the material is probed.

In addition, with increasing Al-loading, the relative number of Al(IV) sites decreases. We suspect that at high loading, the conversion of Al(IV) species into Al(V) is due to the increased ionicity of the framework, leading to preferred higher coordination number. Indeed, intrinsically, the Al–O bond is more ionic than the Si–O bond as expected from the respective electronegativity values of Al, Si, and O and the definition of ionicity given by Pauling.<sup>91–93</sup> Simultaneously, the ratio of six-coordinate Al sites remains at around 60% of the total aluminum atoms.

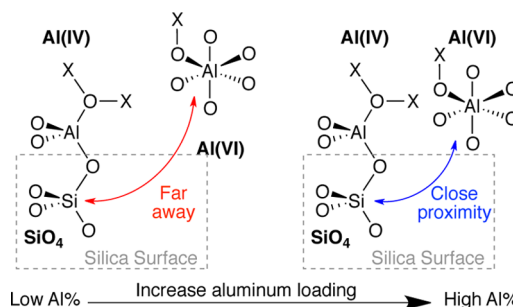
To obtain direct insight into the bonding between Al and  $\text{SiO}_2$ , DNP SENS  $^{29}\text{Si}$ – $^{27}\text{Al}$  INEPT was used to obtain two-dimensional  $^{29}\text{Si}$  and  $^{27}\text{Al}$  heteronuclear correlation (HETCOR) spectra of Al/ $\text{SiO}_2$  (Figure 1C, spectra g–i). We note that the  $^{29}\text{Si}$ – $^{27}\text{Al}$  correlation experiments are very challenging due to the low natural isotopic abundance of  $^{29}\text{Si}$  (natural abundance of 4.7%) and inefficient polarization transfer to or from quadrupolar  $^{27}\text{Al}$  nuclei. Therefore, 2D  $^{29}\text{Si}$ – $^{27}\text{Al}$  correlation experiments were performed at 400 MHz/263 GHz where substantially higher DNP enhancements and NMR sensitivity were obtained. The HETCOR spectra were obtained with  $^{29}\text{Si}$ – $^{27}\text{Al}$  scalar

couplings to selectively observe scalar coupled aluminum and silicon atoms linked by bridging oxygen (black traces). HETCOR spectra were also obtained with  $^{29}\text{Si}$ – $^{27}\text{Al}$  dipolar couplings by applying dipolar recoupling during the evolution period to observe both bonded and nonbonded but proximate aluminum and silicon atoms (red contours/traces). The scalar HETCOR spectra (black contours/traces) indicate that in all cases the silica tetrahedra are primarily bound to aluminum tetrahedra in Al/ $\text{SiO}_2$  (fits of the projected  $^{27}\text{Al}$  dimension for both scalar and dipolar spectrum are provided in the SI, see Figures S8 and S9 and Tables S2 and S3). The dipolar  $^{29}\text{Si}$ – $^{27}\text{Al}$  correlation spectra (Figure 1C, spectra g–i, red traces) show correlations between  $^{29}\text{Si}$   $\text{Q}_4$  sites with  $^{27}\text{Al}$ (IV) and additional weak correlations between silicon and octahedral aluminum Al(VI) in all cases (Figure S9 and Table S3). This result is consistent with earlier NMR analysis on cogelled ASA samples with high silica content.<sup>36</sup> The relative intensity of the latter correlations increases as the aluminum loading level is increased. As the dipolar correlation experiment gives correlations through space, the observed correlations to the octahedral Al-sites are very weak and likely arise from coupling to proximate nonbonded Al-octahedra. Note that at this stage, the correlation with Al(V) nuclei cannot be excluded but does not appear on the correlation plots probably due to low sensitivity of  $^{29}\text{Si}$ – $^{27}\text{Al}$  correlation experiments and the reduced resolution of the  $^{27}\text{Al}$  spectra at 9.4 T. We note that DNP enhanced  $^1\text{H}$ – $^{27}\text{Al}$  and  $^1\text{H}$ – $^{29}\text{Si}$  dipolar HETCOR spectra were also acquired (Figure S10 and S11). However, both the  $^1\text{H}$ – $^{29}\text{Si}$  and  $^1\text{H}$ – $^{27}\text{Al}$  HETCOR spectra generally show correlations to a very broad range of  $^1\text{H}$  chemical shifts (ca. 0.5 to 10 ppm), which likely reflects the diverse range of proton environments at the surface (hydroxyl, water, adsorbed solvent molecules, acidic protons, etc.). The most intense  $^1\text{H}$  peaks in the HETCOR spectra are centered around 4.5–5 ppm and ca. 6.2 ppm. These  $^1\text{H}$  chemical shifts likely correspond to adsorbed  $\text{H}_2\text{O}$  and TCE solvent molecules, respectively. The  $^1\text{H}$  peaks in the HETCOR spectra are also rather featureless, which prevents useful structural information from being obtained.

In summary, the scalar and dipolar DNP SENS  $^{29}\text{Si}$ – $^{27}\text{Al}$  HETCOR spectra indicate that the majority of aluminum species that are bound to the silica surface via Si  $\text{Q}_4$  sites are Al(IV) and as the loading increases the number of Al(VI) proximate to the silica surface increases (Scheme 1).

**Probing the Structure of Silicon on  $\text{Al}_2\text{O}_3$ .** Si/ $\text{Al}_2\text{O}_3$  prepared by the deposition of  $\text{SiO}_2$  on  $\text{Al}_2\text{O}_3$  via a molecular

**Scheme 1.** Representation of the Al/ $\text{SiO}_2$  Interface Depicting Direct Bonding between Tetrahedral Aluminum and Silicon Sites and the Proximity of Octahedral Aluminum Sites<sup>a</sup>



<sup>a</sup>X = Al, Si, or H. Homocondensation of the alkoxides is possible leading to the formation Al–O–Al-type species.

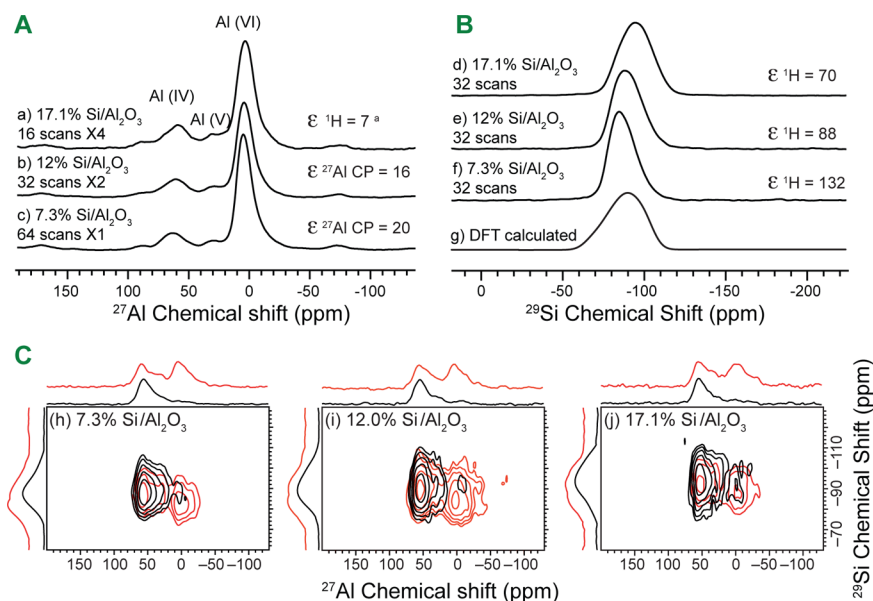


**Figure 2.** (A) DNP enhanced  $^1\text{H}$ - $^{27}\text{Al}$  CPMAS solid-state NMR spectra acquired at 600 MHz/395 GHz: (a) 17.1 wt %  $\text{Si}/\text{Al}_2\text{O}_3$ , (b) 12 wt %  $\text{Si}/\text{Al}_2\text{O}_3$ , and (c) 7.3 wt %  $\text{Si}/\text{Al}_2\text{O}_3$ . Spectra for all of these samples were also measured on a 400 MHz DNP spectrometer (Figure S3, ESI). (B) DNP SENS (400 MHz/263 GHz)  $^1\text{H}$ - $^{29}\text{Si}$  CPMAS solid-state NMR spectra: (d) 17.1 wt %  $\text{Si}/\text{Al}_2\text{O}_3$ , (e) 12 wt %  $\text{Si}/\text{Al}_2\text{O}_3$ , and (f) 7.3 wt %  $\text{Si}/\text{Al}_2\text{O}_3$ . For  $^{29}\text{Si}$  measurement, DNP enhancement was measured by directly observing the  $^1\text{H}$  spectrum, since the acquisition of a  $^{29}\text{Si}$  CPMAS spectrum without DNP required too long for signal averaging. (g) DFT calculated spectrum for all  $^{29}\text{Si}$  nuclei, independently of their proximity to  $^1\text{H}$ . The model corresponds to a 14%  $\text{Si}/\text{Al}_2\text{O}_3$ . All spectra were acquired with a 12.5 kHz spinning frequency and a CP contact time of 0.6 ms for  $^{27}\text{Al}$  and 3.0 ms for  $^{29}\text{Si}$ .  $^1\text{H}$ - $^{27}\text{Al}$  CPMAS of the starting alumina is available, Figure S12. (C) DNP SENS (400 MHz/263 GHz) scalar refocused INEPT (black traces/contours) and dipolar refocused  $\text{R}^3$ -INEPT (red traces/contours)  $^{29}\text{Si}$ - $^{27}\text{Al}$  heteronuclear correlation spectra of (h) 17.1 wt %  $\text{Si}/\text{Al}_2\text{O}_3$ , (i) 12 wt %  $\text{Si}/\text{Al}_2\text{O}_3$ , and (j) 7.3 wt %  $\text{Si}/\text{Al}_2\text{O}_3$ . All spectra were acquired with a 12.5 kHz MAS frequency. Projections of the 2D spectra are shown along the horizontal and vertical axes. For dipolar correlation experiments, 96 total rotor cycles ( $N$ , Figure S1) of recoupling were used, while for scalar correlation experiments, 420 total rotor cycles of evolution were used. Spectra were acquired with 16–80 scans per increment, 28  $t_1$  increments, and a rotor synchronized  $t_1$  increment of 80  $\mu\text{s}$ . Recycle delays were optimized for sensitivity and were between 3.8 and 5.0 s. The pulse sequences used to acquire the 2D spectra are illustrated in Figure S1.

approach was also investigated by DNP SENS.  $^1\text{H}$ - $^{27}\text{Al}$  CPMAS spectra were recorded for the  $\text{Si}/\text{Al}_2\text{O}_3$  samples (Figure 2A, spectra a–c). Higher DNP enhancements of 7–20 were obtained for  $\text{Si}/\text{Al}_2\text{O}_3$  compared with enhancements of 5–8 observed for  $\text{Al}/\text{SiO}_2$  at 600 MHz/395 GHz. The larger enhancements observed for  $\text{Si}/\text{Al}_2\text{O}_3$  samples (51–80 at 400 MHz/263 GHz) compared with  $\text{Al}/\text{SiO}_2$  ( $\epsilon_{\text{Al-CP}}$  of 114–153 at 400 MHz/263 GHz) could reflect more suitable dielectric properties of alumina.<sup>69</sup> However, other factors such as the degree of oxygen removal<sup>69</sup> or interaction or aggregation of the radicals could also impact the observed DNP enhancements. Once again, three distinct resonances centered around 9, 36, and 65 ppm were observed in the  $^1\text{H}$ - $^{27}\text{Al}$  CPMAS spectra and are assigned to Al(VI), Al(V), and Al(IV) aluminum atoms in agreement with DFT calculations (Table S4). Given the sensitivity of the  $^{27}\text{Al}$  NMR chemical shifts and quadrupole parameters to hydration and the challenge of accurately modeling water coordination/hydration of the surface, we did not consider the calculated  $^{27}\text{Al}$  NMR spectra.<sup>66</sup>

Fits of the  $^{27}\text{Al}$  CPMAS spectra show that the relative ratio of the Al(VI)/Al(V)/Al(IV) sites is approximately 75:5:20 for all silica loading levels. There is not a strong variation in the relative intensities of the different aluminum sites with increasing  $\text{SiO}_2$  loading level (Figure S13 and Table S5). However, as the loading of  $\text{SiO}_2$  is increased and the alumina surface becomes covered, the absolute intensity of the  $^{27}\text{Al}$  CPMAS spectra is observed to decrease (Figure S3). In addition, we may also expect a different intrinsic behavior of  $\text{Al}/\text{SiO}_2$  and  $\text{Si}/\text{Al}_2\text{O}_3$  interfaces. In  $\text{Si}/\text{Al}_2\text{O}_3$ , we expect that Al(V) sites result from the reconstruction–

amorphization process as reported in ref 19; the rigid alumina framework imposes structural constraints and likely limits the formation of a large number of Al(V) even at high silica content. In contrast for  $\text{Al}/\text{SiO}_2$ , monomeric aluminum species deposited on the silica surface are intrinsically more flexible, thus allowing the formation of Al(V) from Al(IV) species (*vide supra*).

Once again, high-quality  $^1\text{H}$ - $^{29}\text{Si}$  CPMAS spectra could be rapidly acquired (ca. 5 min for a one-dimensional spectrum). The DNP enhanced  $^1\text{H}$ - $^{29}\text{Si}$  CPMAS spectra of  $\text{Si}/\text{Al}_2\text{O}_3$  are shown for three different silicon loadings of 7.3, 12.0, and 17.1 wt % (Figure 2B, spectra d–f). The  $^{29}\text{Si}$  DNP SENS CPMAS spectra of  $\text{Si}/\text{Al}_2\text{O}_3$  can be decomposed into three components at –83, –93, and –100 ppm (Figure S14 and S15).

The calculated  $^{29}\text{Si}$  chemical shifts of the various surface sites are distributed between –78 and –99 ppm, consistent with the experimental observations. Applying Gaussian broadening to this distribution leads to the simulated spectrum reported in Figure 2B, trace g. The position of the maximum is enclosed between those of the experimental spectra of the 12% and 17.1%  $\text{Si}/\text{Al}_2\text{O}_3$  sample. The DFT model is representative of a perfectly dispersed silica overlayer, without multilayers, which may explain the slightly different shape of the simulated spectrum compared with the experiment; the DFT simulated spectrum is slightly more intense at negative chemical shifts and less intense at the more positive chemical shift tail (Figure S16). Reducing the broadening for the simulated spectrum leads to a three-component spectrum (Figure S17), centered at around –80, –92, and –97 ppm. Excluding the Si atoms that do not have any hydrogen as second neighbors from the simulation does not affect the shape

of the spectrum. All surface Si are likely observed since the contact time used for the  $^1\text{H}$ – $^{29}\text{Si}$  CPMAS experiment is long (3 ms).

On the basis of DFT calculations, we can propose an assignment of the spectra of the  $\text{Si}/\text{Al}_2\text{O}_3$  samples. Note however that the presence of various environments around similar  $^{29}\text{Si}$  (Figure 3), for example, various Si–O–Si and Si–O–Al angles

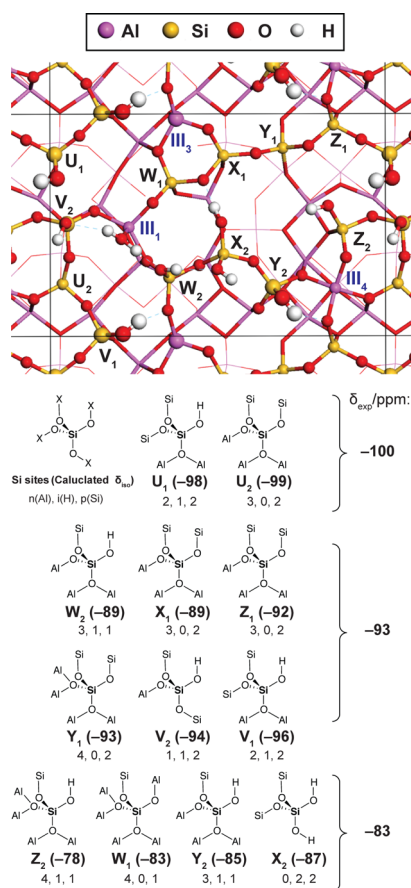


**Figure 3.** On the top, top view of the  $\text{Si}/\text{Al}_2\text{O}_3$  DFT model employed with  $\theta_{\text{OH}} = 5.4 \text{ nm}^{-2}$ , constructed from the silication of the (100)  $\gamma$ - $\text{Al}_2\text{O}_3$  surface. The terminology for Si and outermost surface Al atoms is given in black and blue, respectively. See Figure S2 and Table S4 (ESI) for more details on local environments and side views. On the bottom, schematic representation of each Si site with the DFT-computed  $^{29}\text{Si}$  chemical shifts in parentheses and the number and the nature of second neighbors for each Si atom on the ASA model employed. The environment of Si is noted  $\text{Si}(n\text{Al}, i\text{H}, p\text{Si})$ , by extension of the terminology from previous work;<sup>89</sup>  $n + i + p$  can be larger than four because of the significant ionicity of the framework (some oxygen are more than 2-fold coordinated). According to the decomposition, DFT calculated peaks were lumped into three subgroups centered around the experimental peaks:  $\delta < -96 \text{ ppm}$ ;  $-96 \text{ ppm} \leq \delta \leq -88 \text{ ppm}$ ;  $-88 \text{ ppm} < \delta$ .

and bond lengths, coordination numbers of Al atoms, presence of additional Al atoms noncovalently bonded but in close proximity to Si–O, will lead to a distribution of chemical shifts, only modeled in part here. In agreement with previous empirical assignments, based on the analysis of crystalline and amorphous aluminosilicates,<sup>85–89</sup> both H and Al second neighbors are at the origin of the increase of the chemical shift of  $^{29}\text{Si}$  nucleus (Figure 4): the  $Z_2$  site, corresponding to  $-78 \text{ ppm}$  chemical shift, is surrounded by the highest number of Al neighbors ( $n = 4$ )

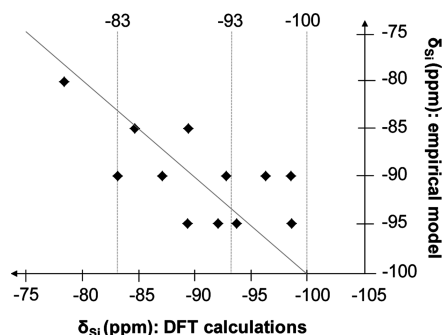


**Figure 4.** Comparison of  $^{29}\text{Si}$  chemical shifts calculated by DFT and an empirical model (see Figure S18), derived from the analysis of the literature data available, assuming 2-fold coordination for all O atoms, and constant chemical shift variation by +10 ppm for each  $^1\text{H}$  and +5 ppm for each Al second neighbor.<sup>85–89</sup> The experimental  $^{29}\text{Si}$  chemical shifts of our  $\text{Si}/\text{Al}_2\text{O}_3$  samples are represented with the dotted vertical lines. The plain line depicts the diagonal of the parity plot.

together with a proton.<sup>85–88</sup> Considering that all oxygen atoms surrounding a Si atom are 2-fold coordinated (as in silica), an empirical assignment (Figure S18) and model (Figure 4) can be drawn for each Si atom in silicates based on the number of H ( $i$ ) and Al ( $n$ ) neighbors, where the chemical shift of a specific Si site is positively shifted by  $(10i + 5n) \text{ ppm}$  from the chemical shift of pure  $\text{SiO}_2$  ( $Q_4$  sites,  $\delta_{\text{iso}} = -110 \text{ ppm}$ ) as a reference (see eq 1).<sup>85–88</sup>

$$\delta_{\text{iso}}(^{29}\text{Si}(i, n)) = ((10i + 5n) - 110) \text{ ppm} \quad (1)$$

However, in the presence of alumina, a more ionic support than silica, oxygen atoms can adopt higher than 2-fold coordination. In alumina, the coordination number of oxygen atoms can be as high as four, so that higher coordination may be expected at the Si/Al interface. If we denote the environment of a given Si as  $\text{Si}(n\text{Al}, i\text{H}, p\text{Si})$  to note the number of its second neighbors, DFT calculations show that  $n + i + p$  can exceed four. This can be related to the so-called “O tricluster” suspected for aluminosilicate glasses.<sup>4,65,94–96</sup> We can extend this concept to an “O tetracluster” on our silicate alumina surface model. This leads to a deviation (below 10 ppm) of the empirical model chemical shifts (Figure 4) since the  $^{29}\text{Si}$  chemical shift cannot be simply related to the nature and number of second neighbors.

To assign the experimental  $^{29}\text{Si}$  CPMAS NMR spectra, we compared the DFT calculated chemical shifts to the three experimental chemical shifts obtained from deconvolution of the  $^{29}\text{Si}$  CPMAS spectrum of 17.1%  $\text{Si}/\text{Al}_2\text{O}_3$  (Figure 3). The  $-93$  and  $-100 \text{ ppm}$  peaks are clearly related to a higher number of Si atoms as second neighbors than the  $-83 \text{ ppm}$  peak. The  $-83$  and  $-93 \text{ ppm}$  peaks correspond generally, but not necessarily, to a high number of Al as second neighbors (for example,  $X_2$ ), since several H as second neighbors can also lead to increase in chemical shifts.<sup>88</sup> Experimental evaluation of the peak intensities shows that at high silicon loading, Si species giving a signal around  $-93 \text{ ppm}$  (and to a lower extent,  $-100 \text{ ppm}$ ) become dominant, whereas the  $-83 \text{ ppm}$  signal vanishes, consistent with the existence of more numerous Si as second neighbors. This can be related to the formation of a  $\text{SiO}_2$  multilayer and a pure silica network (Figure S14). At low loading, the  $-83 \text{ ppm}$  peak increases dramatically, consistent with the first layer of silicate bonding directly to the surface of  $\text{Al}_2\text{O}_3$ .

Scalar two-dimensional  $^{29}\text{Si}$ – $^{27}\text{Al}$  DNP SENS INEPT HETCOR spectra of  $\text{Si}/\text{Al}_2\text{O}_3$  (Figure 2C, spectra h–j) show



that the silica tetrahedra are primarily bonded to the aluminum tetrahedra (decompositions of the projection of the  $^{27}\text{Al}$  dimension for both scalar and dipolar HETCOR spectra are given in Figures S8 and S9 and Tables S2 and S3). However, in the scalar HETCOR spectra, weak correlations to octahedral aluminum sites are observed, and the relative intensities of these correlations are constant (within the uncertainty of the measurement) with increasing loading of Si on alumina (Figure S8 and Table S2). This is consistent with the high intensity of the octahedral aluminum sites observed in the 1D  $^{27}\text{Al}$  CPMAS spectra of  $\text{Si}/\text{Al}_2\text{O}_3$ . The dipolar  $^{29}\text{Si}$ – $^{27}\text{Al}$  HETCOR spectra of  $\text{Si}/\text{Al}_2\text{O}_3$  show more intense correlations to octahedral aluminum sites and penta-coordinate aluminum, in particular for the lowest Si loading. The relative intensity of the correlations to the octahedral and penta-coordinate aluminum sites is also increased in  $\text{Si}/\text{Al}_2\text{O}_3$  compared with the corresponding HETCOR spectra of  $\text{Al}/\text{SiO}_2$  due to the presence of 6- and 5-fold coordination of aluminum sites on the alumina surface and therefore the close proximity with the  $^{29}\text{Si}$  nuclei (Figure S9 and Table S3). To explain this, we analyzed the Si to Al proximity in our DFT model (Figure S19). From this, we expect correlations with all types of Al atoms (IV, V, VI), but clearly the environment of Si is richer in Al(IV) than *a priori* expected from the structure of the alumina surface (on the (100) alumina orientation used for the simulation, no Al(IV) are exposed at the surface).<sup>76,77</sup> This can be interpreted as an Al(VI) to Al(IV) and Al(V) to Al(IV) conversion induced by silica. This conversion is likely driven by the higher degree of covalence of silica compared with alumina, which favors lower coordination numbers. This is in line with the higher Al(IV)/Al(VI) ratio observed as silica content increases in ASA, which was known from classical  $^{27}\text{Al}$  NMR.<sup>18,37,38</sup> Note that the Al(IV) giving signal in the  $^{29}\text{Si}$ – $^{27}\text{Al}$  HETCOR spectra (Figures 1C and 2C) appears at slightly lower isotropic chemical shifts (62–66 ppm, Figure S9 and Table S3) than in the 1D DNP enhanced  $^{27}\text{Al}$  CPMAS NMR spectra (66–73 ppm, Figure S13 and Table S5). This can be related to the DFT results, which show that the isotropic chemical shift of Al(IV) is reduced when silicon is present as second neighbor (Figure 5). This is

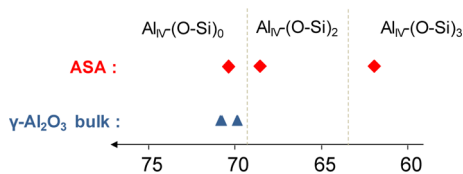


**Figure 5.** DFT calculated dependence on Al(IV) isotropic chemical shift as a function of the number of Si as second neighbors of Al.  $\gamma\text{-Al}_2\text{O}_3$  serves as reference with no Si as second neighbors. In  $\text{Al}_{\text{IV}}-(\text{OSi})_x$ , IV refers tetracoordinate aluminum and  $x$  to the number of (OSi) bound to Al.

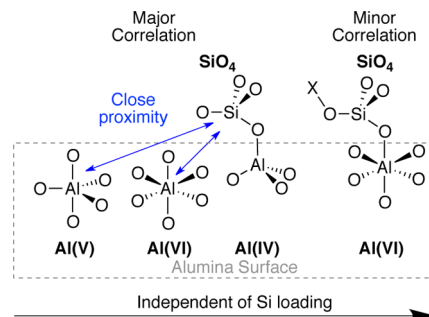
qualitatively comparable to observations from calculations on aluminosilicate glasses, even if the strength of the effect is different.<sup>90</sup> Note also that the  $^{29}\text{Si}$  nuclei detected in  $^{29}\text{Si}$ – $^{27}\text{Al}$  HETCOR appear at more positive chemical shifts than those in the 1D  $^{29}\text{Si}$  CPMAS NMR spectrum. This is because Si sites that neighbor Al will give rise to more positive  $^{29}\text{Si}$  chemical shifts than Si near to only Si.

In summary, the 1D  $^{27}\text{Al}$  and  $^{29}\text{Si}$  and 2D  $^{29}\text{Si}$ – $^{27}\text{Al}$  correlation spectra suggest that grafting of silica onto alumina primarily results in the formation of bonds between  $\text{SiO}_4$  tetrahedra and tetrahedral Al(IV) sites; however, some  $\text{SiO}_4$  tetrahedra are bonded to octahedral Al sites. Since  $\text{SiO}_2$  is deposited onto

$\text{Al}_2\text{O}_3$ , most Si atoms will be proximate to the aluminum surface resulting in more intense correlations between Si and octahedral and penta-coordinated aluminum atoms. The observation of more negative  $^{29}\text{Si}$  chemical shifts with increasing Si loading level is also consistent with formation of a  $\text{SiO}_2$  multilayer at higher loading level.

Taken together, the variation in the intensities of the DNP SENS 1D and 2D NMR with the loading levels can be used to propose some simple structural models (Scheme 2). On Si/

**Scheme 2.** Representation of the Si/ $\text{Al}_2\text{O}_3$  Interface Depicting Direct Bonding between Tetrahedral Aluminum Silicon Sites and Close Proximity of Octahedral Aluminum Sites<sup>a</sup>



<sup>a</sup>X = Al, Si, or H. Homocondensation of the alkoxides is possible leading to the formation Si–O–Si-type species.

$\text{Al}_2\text{O}_3$ , the population of Al(VI) is more abundant than on Al/ $\text{SiO}_2$  (from  $^{27}\text{Al}$  DNP SENS). Many Si nuclei are bonded to OH groups and are connected to Al(IV) as second neighbors, being also quite close to Al(VI) and Al(V) species. This strong connection to Al(IV) atoms is linked to the locally strong covalence of ASA compared with alumina. As the silica loading increases, there is an overall increase in the intensity of signal with more negative chemical shifts. This suggests that increasing loading of  $\text{SiO}_2$  results in the formation of a  $\text{SiO}_2$  multilayer, likely a pure silica network. On the other hand, when Al is grafted onto silica in Al/ $\text{SiO}_2$ , the relative intensity of the tetrahedral sites is higher, due to the high covalence of the host matrix (silica). However, as the Al-loading increases, an  $\text{Al}_2\text{O}_3$  overlayer begins to form and relative ratio of tetrahedral to six-coordinate sites decreases to converge toward that of pure  $\gamma$ -alumina (3/1). Interestingly, the relative amount of penta-coordinated aluminum sites at the surface increases with the grafting of alumina, suggesting that more defected alumina surface sites may result as the loading level is increased, thereby confirming previous propositions.<sup>32</sup>

**Relation to Brønsted acidity.** The present NMR data, in particular the correlation experiments, yield new insight into the atomistic structure of the Brønsted acid sites of ASA materials. Table 2 quantifies the Brønsted acid sites.<sup>16,31–33</sup> On Al/ $\text{SiO}_2$  samples, the occurrence of Si(IV)–Al(IV) connectivity as the aluminum loading increases is associated with a higher concentration of acid sites per Al atom on these samples.<sup>33</sup> Previous measurements of the concentration of Brønsted acid sites have shown that there are more Brønsted acid sites per deposited aluminum at low Al loading levels. The DNP SENS  $^{27}\text{Al}$  CPMAS spectra also show that there is an increase in the relative amount of Al(IV) sites at low loading levels. Taken together, these two results strongly suggest that the formation of Brønsted acid sites is related to the presence of Al(IV) on the Al/ $\text{SiO}_2$  surface. This finding substantiates previous observations.<sup>97</sup>

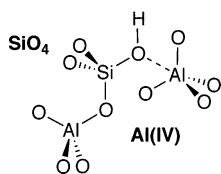
**Table 2. Coverage by Aluminum Species and Surface Density of Brønsted Acid Sites**<sup>31,33</sup>

sample	Brønsted acid sites (nm <sup>-2</sup> )	Brønsted acid sites per Al atom (× 10 <sup>-2</sup> , Al exposed <sup>-1</sup> )
5.7% Al <sub>2</sub> O <sub>3</sub> /SiO <sub>2</sub>	0.20	15.4
15% Al <sub>2</sub> O <sub>3</sub> /SiO <sub>2</sub>	0.39	6.7
24.8% Al <sub>2</sub> O <sub>3</sub> /SiO <sub>2</sub>	0.52	7.3
7.3% SiO <sub>2</sub> /Al <sub>2</sub> O <sub>3</sub>	0.04	0.5
12% SiO <sub>2</sub> /Al <sub>2</sub> O <sub>3</sub>	0.11	1.5
17.1% SiO <sub>2</sub> /Al <sub>2</sub> O <sub>3</sub>	0.19	5.2

Silicon connected to aluminum with higher coordination number would be inefficient in forming Brønsted acid sites.

The results on Al/SiO<sub>2</sub> materials show that the low coordination of the aluminum atoms and the presence of silica as a matrix are both crucial parameters for obtaining Brønsted acid sites in ASAs. Gathering such conditions by grafting silicon species on the Al<sub>2</sub>O<sub>3</sub> surface is more difficult for two main reasons. On the one hand, the coordination of the aluminum atoms populating the Al<sub>2</sub>O<sub>3</sub> surface is on average closer to six than to four, higher than that of the first aluminum species deposited in Al/SiO<sub>2</sub> samples. On the other hand, a significant amount of deposited silicon species is required so as to change the covalence of the surface aluminum species in such a way that it induces the formation of reactive sites. Hence the number of Brønsted acid sites per exposed aluminum atom in Si/Al<sub>2</sub>O<sub>3</sub> samples increases with the silica loading and consequent coverage of aluminum surface species.

Hensen et al.<sup>20</sup> categorized the acid sites of ASAs in two main types, the strongest ones being bridging acid sites such as in zeolites and the milder ones being specific to ASAs with different structures. Experimental and computational data combined suggest that the structures of the acid sites of ASAs are bridging hydroxyl between Si(IV) and Al(IV), possibly associated with pseudo-bridging silanols (PBS) for Si/Al<sub>2</sub>O<sub>3</sub> materials (Scheme 3).<sup>19,29,93,98</sup> Such sites are defined as silanols being noncovalently

**Scheme 3. Proposal for a Possible Structure of Brønsted Acid Sites on ASA (Si/Al<sub>2</sub>O<sub>3</sub>): Pseudo-Bridging Silanol in Connection with Al(IV) Species**

bonded to aluminum atoms (electrostatic interaction between aluminum atoms and oxygen of the silanol, shown as dashed line in Scheme 3). According to calculations, such species can be protonated by basic probe molecules (B) such as lutidine, by closing the Si–O···Al bridge, yielding Si–O–Al anionic species and BH<sup>+</sup>, in agreement with ref 17.<sup>30,93</sup> Moreover, the intrinsic protonation and cracking abilities of such PBS sites have recently been compared with bridging acid sites of a zeolite in DFT calculations, and these specific structures would account for the milder acidity of PBS and corroborate the main role of the interaction between the alumina support and deposited silicon species.<sup>98</sup> In the present work, on the basis of the NMR spectra, we suggest that the acceptor Al atom is likely in tetrahedral coordination and that the silicon bearing the silanol is covalently bonded to other Al(IV) ions (Scheme 3). However, all PBS sites

are covalently connected to only Al(VI) and Al(V) in the DFT model discussed here, due to the high aluminum content. While it is hard to make an unambiguous prediction of the <sup>29</sup>Si NMR chemical shift for sites depicted in Scheme 3, the two PBS sites, V<sub>1</sub> and Z<sub>2</sub> in Figure 3, can be considered as prototypical examples: they are characterized by very distinct calculated chemical shifts of –96 and –78 ppm, respectively. This large difference of calculated chemical shifts for similar species shows that 1D NMR cannot be used to identify the Brønsted acid sites of ASA. In contrast, NMR correlation experiments, which probe Al(IV) to Si(IV) proximity, a requirement for Brønsted acidity, are therefore better suited to characterize such species.

## CONCLUSIONS

Combining DNP SENS NMR, including 2D scalar and dipolar <sup>29</sup>Si–<sup>27</sup>Al INEPT, and DFT calculations on ASA materials has allowed for a detailed atomic level description of (i) the connectivity between Si and Al nuclei on ASA surfaces, as a function of their coordination number and local environment, and (ii) structural insight into the nature of Brønsted acid sites, which unifies the behavior of solids obtained by grafting either Al on silica or Si on alumina.

On silica and alumina surfaces, molecular Si and Al precursors are preferentially grafted as “(IV)-to-(IV)”-coordinated mixed layer: the deposited silicon species are preferentially attached to Al(IV) sites issued from Al atoms of various coordinations of γ-alumina, with strong Si(IV)–Al(IV) connectivity. Similarly, the first deposited aluminum species on silica in Al/SiO<sub>2</sub> are Al(IV) tetrahedrally coordinated species. This specific surface site connectivity eventually enables the formation of Brønsted acid sites. Such acid sites may be formulated as bridging hydroxyls in connection with Al(IV) species, such as pseudo-bridging silanol in Al/SiO<sub>2</sub>. While an atomic level description of the interface of ASAs remains complex because each preparation technique makes a unique structure, the present study lays the foundation for the determination of the structure of the Brønsted active sites in the large family of aluminosilicates with the ultimate goal to establish structure–activity relationships and to use more rational development of solid acid catalysts.

## ASSOCIATED CONTENT

### Supporting Information

The Supporting Information is available free of charge on the ACS Publications website at DOI: 10.1021/jacs.5b06134.

Refocused INEPT pulse sequence, a compilation of <sup>29</sup>Si and <sup>27</sup>Al NMR spectra and their fits, and details on the DFT calculations (PDF)

## AUTHOR INFORMATION

### Corresponding Authors

\*ccoperet@ethz.ch

\*jeroen.vanbokhoven@chem.ethz.ch

### Notes

The authors declare no competing financial interest.

## ACKNOWLEDGMENTS

M.V. thanks the SNF foundation for financial support (Grant No. 200021\_142600). This work was funded in part by the ERC Advanced Grant No. 320860 and SNF equipment grant (206021\_150710).



## REFERENCES

- (1) Corma, A. *Chem. Rev.* **1995**, *95*, 559.
- (2) Busca, G. *Chem. Rev.* **2007**, *107*, 5366.
- (3) Perez-Ramirez, J.; Christensen, C. H.; Egeblad, K.; Christensen, C. H.; Groen, J. C. *Chem. Soc. Rev.* **2008**, *37*, 2530.
- (4) Stebbins, J. F.; Xu, Z. *Nature* **1997**, *390*, 60.
- (5) Moses, A. W.; Raab, C.; Nelson, R. C.; Leifeste, H. D.; Ramsahye, N. A.; Chattopadhyay, S.; Eckert, J.; Chmelka, B. F.; Scott, S. L. *J. Am. Chem. Soc.* **2007**, *129*, 8912.
- (6) Motokura, K.; Tada, M.; Iwasawa, Y. *J. Am. Chem. Soc.* **2007**, *129*, 9540.
- (7) Alphazan, T.; Bonduelle-Skrzypczak, A.; Legens, C. I.; Gay, A.-S.; Boudene, Z.; Girleanu, M.; Ersen, O.; Copéret, C.; Raybaud, P. *ACS Catal.* **2014**, *4*, 4320.
- (8) Bertoncini, F.; Bonduelle-Skrzypczak, A.; Francis, J.; Guillon, E. *Catalysis by Transition Metal Sulphides: From Molecular Theory to Industrial Application*; Raybaud, P.; Toulhoat, H., Eds.; Technip: Paris, 2013; Chapter 3.4, p 609.
- (9) Thieuleux, C.; Maraval, A.; Veyre, L.; Copéret, C.; Soulivong, D.; Basset, J.-M.; Sunley, G. J. *Angew. Chem., Int. Ed.* **2007**, *46*, 2288.
- (10) Weitkamp, J. *ChemCatChem* **2012**, *4*, 292.
- (11) Bond, J. Q.; Alonso, D. M.; Wang, D.; West, R. M.; Dumesic, J. A. *Science* **2010**, *327*, 1110.
- (12) Hahn, M. W.; Copeland, J. R.; van Pelt, A. H.; Sievers, C. *ChemSusChem* **2013**, *6*, 2304.
- (13) Marcilly, C. *J. Catal.* **2003**, *216*, 47.
- (14) Hensen, E. J. M.; Poduval, D. G.; Degirmenci, V.; Ligthart, D. A. J. M.; Chen, W.; Mauge, F.; Rigutto, M. S.; van Veen, J. A. R. *J. Phys. Chem. C* **2012**, *116*, 21416.
- (15) Koekkoek, A. J. J.; van Veen, J. A. R.; Gerritsen, P. B.; Giltay, P.; Magusin, P. C. M. M.; Hensen, E. J. M. *Microporous Mesoporous Mater.* **2012**, *151*, 34.
- (16) Caillot, M.; Chaumonnot, A.; Digne, M.; van Bokhoven, J. A. *J. Catal.* **2014**, *316*, 47.
- (17) Trombetta, M.; Busca, G.; Rossini, S.; Piccoli, V.; Cornaro, U.; Guercio, A.; Catani, R.; Willey, R. J. *J. Catal.* **1998**, *179*, 581.
- (18) Crépeau, G.; Montouillout, V.; Vimont, A.; Mariey, L.; Cseri, T.; Mauté, F. *J. Phys. Chem. B* **2006**, *110*, 15172.
- (19) Chizallet, C.; Raybaud, P. *Angew. Chem., Int. Ed.* **2009**, *48*, 2891.
- (20) Poduval, D. G.; van Veen, J. A. R.; Rigutto, M. S.; Hensen, E. J. M. *Chem. Commun.* **2010**, *46*, 3466.
- (21) Thomas, C. L. *Ind. Eng. Chem.* **1949**, *41*, 2564.
- (22) Tamele, M. W. *Discuss. Faraday Soc.* **1950**, *8*, 270.
- (23) Hansford, R. C. *Ind. Eng. Chem.* **1947**, *39*, 849.
- (24) Xu, B.; Sievers, C.; Lercher, J. A.; van Veen, J. A. R.; Giltay, P.; Prins, R.; van Bokhoven, J. A. *J. Phys. Chem. C* **2007**, *111*, 12075.
- (25) Huang, J.; van Vegten, N.; Jiang, Y.; Hunger, M.; Baiker, A. *Angew. Chem., Int. Ed.* **2010**, *49*, 7776.
- (26) de Boer, J. H. *Discuss. Faraday Soc.* **1971**, *52*, 109.
- (27) Blonski, S.; Garofalini, S. H. *J. Phys. Chem.* **1996**, *100*, 2201.
- (28) Hwang, C.-P.; Yeh, C.-T. *J. Catal.* **1999**, *182*, 48.
- (29) Leydier, F.; Chizallet, C.; Chaumonnot, A.; Digne, M.; Soyer, E.; Quoineaud, A.-A.; Costa, D.; Raybaud, P. *J. Catal.* **2011**, *284*, 215.
- (30) Leydier, F.; Chizallet, C.; Costa, D.; Raybaud, P. *Chem. Commun.* **2012**, *48*, 4076.
- (31) Caillot, M.; Chaumonnot, A.; Digne, M.; Bokhoven, J. A. V. *ChemCatChem* **2013**, *5*, 3644.
- (32) Caillot, M.; Chaumonnot, A.; Digne, M.; Poleunis, C.; Debecker, D. P.; van Bokhoven, J. A. *Microporous Mesoporous Mater.* **2014**, *185*, 179.
- (33) Caillot, M.; Chaumonnot, A.; Digne, M.; Van Bokhoven, J. A. *ChemCatChem* **2014**, *6*, 832.
- (34) Toulhoat, H.; Raybaud, P.; Benazzi, E. *J. Catal.* **2004**, *221*, 500.
- (35) Gilson, J.-P.; Edwards, G. C.; Peters, A. W.; Rajagopalan, K.; Wormsbecher, R. F.; Roberie, T. G.; Shatlock, M. P. *J. Chem. Soc., Chem. Commun.* **1987**, 91.
- (36) Man, P. P.; Peltre, M. J.; Barthomeuf, D. *J. Chem. Soc., Faraday Trans.* **1990**, *86*, 1599.
- (37) Dorémieux-Morin, C.; Martin, C.; Brégeault, J.-M.; Fraissard, J. *Appl. Catal.* **1991**, *77*, 149.
- (38) De Witte, B. M.; Grobet, P. J.; Uytterhoeven, J. B. *J. Phys. Chem.* **1995**, *99*, 6961.
- (39) Omegna, A.; van Bokhoven, J. A.; Prins, R. *J. Phys. Chem. B* **2003**, *107*, 8854.
- (40) Lesage, A.; Lelli, M.; Gajan, D.; Caporini, M. A.; Vitzthum, V.; Miéville, P.; Alauzun, J.; Roussey, A.; Thieuleux, C.; Mehdi, A.; Bodenhausen, G.; Copéret, C.; Emsley, L. *J. Am. Chem. Soc.* **2010**, *132*, 15459.
- (41) Lelli, M.; Gajan, D.; Lesage, A.; Caporini, M. A.; Vitzthum, V.; Miéville, P.; Héroguel, F.; Rascon, F.; Roussey, A.; Thieuleux, C.; Boualleg, M.; Veyre, L.; Bodenhausen, G.; Coperet, C.; Emsley, L. *J. Am. Chem. Soc.* **2011**, *133*, 2104.
- (42) Rossini, A. J.; Zagdoun, A.; Lelli, M.; Lesage, A.; Copéret, C.; Emsley, L. *Acc. Chem. Res.* **2013**, *46*, 1942.
- (43) Song, C.; Hu, K.-N.; Joo, C.-G.; Swager, T. M.; Griffin, R. G. *J. Am. Chem. Soc.* **2006**, *128*, 11385.
- (44) Maly, T.; Debelouchina, G. T.; Bajaj, V. S.; Hu, K.-N.; Joo, C.-G.; Mak-Jurkauskas, M. L.; Sirigiri, J. R.; van der Wel, P. C. A.; Herzfeld, J.; Temkin, R. J.; Griffin, R. G. *J. Chem. Phys.* **2008**, *128*, 052211.
- (45) Ni, Q. Z.; Daviso, E.; Can, T. V.; Markhasin, E.; Jawla, S. K.; Swager, T. M.; Temkin, R. J.; Herzfeld, J.; Griffin, R. G. *Acc. Chem. Res.* **2013**, *46*, 1933.
- (46) Pines, A.; Gibby, M. G.; Waugh, J. S. *J. Chem. Phys.* **1972**, *56*, 1776.
- (47) Zagdoun, A.; Casano, G.; Ouari, O.; Lapadula, G.; Rossini, A. J.; Lelli, M.; Baffert, M.; Gajan, D.; Veyre, L.; Maas, W. E.; Rosay, M.; Weber, R. T.; Thieuleux, C.; Coperet, C.; Lesage, A.; Tordo, P.; Emsley, L. *J. Am. Chem. Soc.* **2012**, *134*, 2284.
- (48) Perras, F. A.; Kobayashi, T.; Pruski, M. *J. Am. Chem. Soc.* **2015**, *137*, 8336.
- (49) Rossini, A. J.; Zagdoun, A.; Lelli, M.; Gajan, D.; Rascon, F.; Rosay, M.; Maas, W. E.; Coperet, C.; Lesage, A.; Emsley, L. *Chem. Sci.* **2012**, *3*, 108.
- (50) Kobayashi, T.; Lafon, O.; Lilly Thankamony, A. S.; Slowing, I. I.; Kandel, K.; Carnevale, D.; Vitzthum, V.; Vezin, H.; Amoureux, J.-P.; Bodenhausen, G.; Pruski, M. *Phys. Chem. Chem. Phys.* **2013**, *15*, 5553.
- (51) Vitzthum, V.; Mieville, P.; Carnevale, D.; Caporini, M. A.; Gajan, D.; Copéret, C.; Lelli, M.; Zagdoun, A.; Rossini, A. J.; Lesage, A.; Emsley, L.; Bodenhausen, G. *Chem. Commun.* **2012**, *48*, 1988.
- (52) Lafon, O.; Thankamony, A. S. L.; Kobayashi, T.; Carnevale, D.; Vitzthum, V.; Slowing, I. I.; Kandel, K.; Vezin, H.; Amoureux, J.-P.; Bodenhausen, G.; Pruski, M. *J. Phys. Chem. C* **2013**, *117*, 1375.
- (53) Wolf, P.; Valla, M.; Rossini, A. J.; Comas-Vives, A.; Núñez-Zarur, F.; Malaman, B.; Lesage, A.; Emsley, L.; Copéret, C.; Hermans, I. *Angew. Chem., Int. Ed.* **2014**, *53*, 10179.
- (54) Gunther, W. R.; Michaelis, V. K.; Caporini, M. A.; Griffin, R. G.; Román-Leshkov, Y. *J. Am. Chem. Soc.* **2014**, *136*, 6219.
- (55) Lee, D.; Duong, N. T.; Lafon, O.; De Paëpe, G. *J. Phys. Chem. C* **2014**, *118*, 25065.
- (56) Lee, D.; Monin, G.; Duong, N. T.; Lopez, I. Z.; Bardet, M.; Mareau, V.; Gonon, L.; De Paëpe, G. *J. Am. Chem. Soc.* **2014**, *136*, 13781.
- (57) Lee, D.; Hediger, S.; De Paëpe, G. *Solid State Nucl. Magn. Reson.* **2015**, *66–67*, 6.
- (58) Profeta, M.; Benoit, M.; Mauri, F.; Pickard, C. J. *J. Am. Chem. Soc.* **2004**, *126*, 12628.
- (59) Gervais, C.; Profeta, M.; Babonneau, F.; Pickard, C. J.; Mauri, F. *J. Phys. Chem. B* **2004**, *108*, 13249.
- (60) Kučera, J.; Nachtigall, P. *Microporous Mesoporous Mater.* **2005**, *85*, 279.
- (61) Chizallet, C.; Costentin, G.; Lauron-Pernot, H.; Che, M.; Bonhomme, C.; Maquet, J.; Delbecq, F.; Sautet, P. *J. Phys. Chem. C* **2007**, *111*, 18279.
- (62) Sklenak, S.; Dědeček, J.; Li, C.; Wichterlová, B.; Gábová, V.; Sierka, M.; Sauer, J. *Angew. Chem., Int. Ed.* **2007**, *46*, 7286.
- (63) Tielens, F.; Gervais, C.; Lambert, J. F.; Mauri, F.; Costa, D. *Chem. Mater.* **2008**, *20*, 3336.
- (64) Brouwer, D. H.; Cadars, S.; Eckert, J.; Liu, Z.; Terasaki, O.; Chmelka, B. F. *J. Am. Chem. Soc.* **2013**, *135*, 5641.

- (65) Charpentier, T.; Menziani, M. C.; Pedone, A. *RSC Adv.* **2013**, 3, 10550.
- (66) Wischert, R.; Florian, P.; Copéret, C.; Massiot, D.; Sautet, P. *J. Phys. Chem. C* **2014**, 118, 15292.
- (67) Zagdoun, A.; Casano, G.; Ouari, O.; Schwarzwälder, M.; Rossini, A. J.; Aussenac, F.; Yulikov, M.; Jeschke, G.; Copéret, C.; Lesage, A.; Tordo, P.; Emsley, L. *J. Am. Chem. Soc.* **2013**, 135, 12790.
- (68) Zagdoun, A.; Rossini, A. J.; Gajan, D.; Bourdolle, A.; Ouari, O.; Rosay, M.; Maas, W. E.; Tordo, P.; Lelli, M.; Emsley, L.; Lesage, A.; Coperet, C. *Chem. Commun.* **2012**, 48, 654.
- (69) Kubicki, D. J.; Rossini, A. J.; Pura, A.; Zagdoun, A.; Ouari, O.; Tordo, P.; Engelke, F.; Lesage, A.; Emsley, L. *J. Am. Chem. Soc.* **2014**, 136, 15711.
- (70) Rosay, M.; Tometich, L.; Pawsey, S.; Bader, R.; Schauwecker, R.; Blank, M.; Borchard, P. M.; Cauffman, S. R.; Felch, K. L.; Weber, R. T.; Temkin, R. J.; Griffin, R. G.; Maas, W. E. *Phys. Chem. Chem. Phys.* **2010**, 12, 5850.
- (71) Trebosc, J.; Hu, B.; Amoureux, J. P.; Gan, Z. *J. Magn. Reson.* **2007**, 186, 220.
- (72) Oas, T. G.; Griffin, R. G.; Levitt, M. H. *J. Chem. Phys.* **1988**, 89, 692.
- (73) Wang, Q.; Trebosc, J.; Li, Y.; Xu, J.; Hu, B.; Feng, N.; Chen, Q.; Lafon, O.; Amoureux, J.-P.; Deng, F. *Chem. Commun.* **2013**, 49, 6653.
- (74) Elena, B.; de Paëpe, G.; Emsley, L. *Chem. Phys. Lett.* **2004**, 398, 532.
- (75) Massiot, D.; Fayon, F.; Capron, M.; King, I.; Le Calvé, S.; Alonso, B.; Durand, J.-O.; Bujoli, B.; Gan, Z.; Hoatson, G. *Magn. Reson. Chem.* **2002**, 40, 70.
- (76) Digne, M.; Sautet, P.; Raybaud, P.; Euzen, P.; Toulhoat, H. *J. Catal.* **2002**, 211, 1.
- (77) Digne, M.; Sautet, P.; Raybaud, P.; Euzen, P.; Toulhoat, H. *J. Catal.* **2004**, 226, 54.
- (78) Clark, S. J.; Segall, M. D.; Pickard, C. J.; Hasnip, P. J.; Probert, M. I. J.; Refson, K.; Payne, M. C. *Z. Kristallogr.* **2005**, 220, 567.
- (79) Perdew, J. P.; Burke, K.; Ernzerhof, M. *Phys. Rev. Lett.* **1996**, 77, 3865.
- (80) Yates, J. R.; Pickard, C. J.; Mauri, F. *Phys. Rev. B: Condens. Matter Mater. Phys.* **2007**, 76, 024401.
- (81) Pickard, C. J.; Mauri, F. *Phys. Rev. B: Condens. Matter Mater. Phys.* **2001**, 63, 245101.
- (82) Kunath-Fandrei, G.; Bastow, T. J.; Hall, J. S.; Jaeger, C.; Smith, M. E. *J. Phys. Chem.* **1995**, 99, 15138.
- (83) Lee, S. K.; Park, S. Y.; Yi, Y. S.; Moon, J. *J. Phys. Chem. C* **2010**, 114, 13890.
- (84) Sarou-Kanian, V.; Gleizes, A. N.; Florian, P.; Samélor, D.; Massiot, D.; Vahlas, C. *J. Phys. Chem. C* **2013**, 117, 21965.
- (85) Lippmaa, E.; Maegi, M.; Samoson, A.; Engelhardt, G.; Grimmer, A. R. *J. Am. Chem. Soc.* **1980**, 102, 4889.
- (86) Lippmaa, E.; Maegi, M.; Samoson, A.; Tarmak, M.; Engelhardt, G. *J. Am. Chem. Soc.* **1981**, 103, 4992.
- (87) Murdoch, J. B.; Stebbins, J. F.; Carmichael, I. S. E. *Am. Mineral.* **1985**, 70, 332.
- (88) Maciel, G. E.; Sindorf, D. W. *J. Am. Chem. Soc.* **1980**, 102, 7606.
- (89) Sato, S.; Sodesawa, T.; Nozaki, F.; Shoji, H. *J. Mol. Catal.* **1991**, 66, 343.
- (90) Gambuzzi, E.; Pedone, A.; Menziani, M. C.; Angeli, F.; Caurant, D.; Charpentier, T. *Geochim. Cosmochim. Acta* **2014**, 125, 170.
- (91) Pauling, L. *The Nature of the Chemical Bond and the Structure of Molecules and Crystals: An Introduction to Modern Structural Chemistry*; Cornell University Press: Ithaca, NY, 1960.
- (92) Chizallet, C.; Digne, M.; Arrouel, C.; Raybaud, P.; Delbecq, F.; Costentin, G.; Che, M.; Sautet, P.; Toulhoat, H. *Top. Catal.* **2009**, 52, 1005.
- (93) Chizallet, C.; Raybaud, P. *ChemPhysChem* **2010**, 11, 105.
- (94) Farnan, I. *Nature* **1997**, 390, 14.
- (95) Benoit, M.; Ispas, S.; Tuckerman, M. E. *Phys. Rev. B: Condens. Matter Mater. Phys.* **2001**, 64, 224205.
- (96) Benoit, M.; Profeta, M.; Mauri, F.; Pickard, C. J.; Tuckerman, M. E. *J. Phys. Chem. B* **2005**, 109, 6052.
- (97) Védérine, J.; Barthomeuf, D.; Dalmai, G.; Trambouze, Y.; Imelik, B.; Prettre, M. C. *R. Acad. Sci. Paris* **1968**, 267, 118.
- (98) Leydier, F.; Chizallet, C.; Costa, D.; Raybaud, P. *J. Catal.* **2015**, 325, 35.